Short-range order and phase stability of CrCoNi explored with machine learning potentials

Sheuly Ghosh [1,*] Vadim Sotskov [2] Alexander V. Shapeev [2] Jörg Neugebauer [1] and Fritz Körmann [1,3]

[1] *Computational Materials Design, Max-Planck-Institut für Eisenforschung GmbH, D-40237 Düsseldorf, Germany*

[2] *Skolkovo Institute of Science and Technology, Bolshoy Boulevard 30, bld. 1, 121205 Moscow, Russia*

[3] *Materials Science and Engineering, Delft University of Technology, 2628 CD Delft, The Netherlands*

(Received 3 June 2022; accepted 2 November 2022; published 30 November 2022)

We present an analysis of temperature-dependent atomic short-range ordering and phase stability of the face-centered cubic CrCoNi medium-entropy alloy employing a combination of *ab initio* calculations and on-lattice machine learning interatomic potentials. Temperature-dependent properties are studied with canonical Monte Carlo simulations. At around 975 K a phase transition into an ordered $Cr(Ni, Co)_2$ phase ($MoPt_2$-type) is found. This hitherto not reported state has an ordering energy twice as large than the ordered structures previously suggested. We show that magnetism is not responsible for the observed chemical ordering.

DOI: 10.1103/PhysRevMaterials.6.113804

I. INTRODUCTION

The concept of multiple-principal element alloys (MPEAs) has raised increasing interest of the scientific and engineering communities over the past decades due to their huge unexplored compositional space and their superior physical, mechanical, environmental, and functional properties [1–8]. Due to their high degree of configurational entropy, MPEAs in high concentrations are often classified as medium-entropy alloys in ternary systems or high-entropy alloys for quaternary or quinary systems and beyond. Many of such alloys have shown extraordinary material properties such as high-cryogenic strength, ductility, toughness, and resistance to corrosion, wear, and fatigue [9–22].

The solid solutions of these multicomponent alloys are often assumed to be ideally random. This may be a reasonable approximation at high temperatures, where configurational entropy dominates the free energy and stabilizes the random alloy. However, atomic-scale short-range ordering (SRO) is, to some degree, always present and can in principle impact thermodynamic quantities and phase stabilities. Recent experiments and simulations indicated that SRO can also impact magnetic [23–25] and mechanical properties [26–30]. It is therefore important to quantify the temperature-dependent ordering behavior rigorously in such alloys.

A tendency for SRO has been suggested in several investigations on different MPEAs [23,31–41]. In the present work, we focus on the prototypical CrCoNi medium-entropy alloy, in which the presence of SRO and its impact on different aspects have been intensively discussed [42–49]. Initial experimental phase diagram determinations showed that the equimolar CrCoNi alloy can form a solid solution on the face-centered cubic (FCC) lattice [50–52], but no information on the possible occurrence of SRO was available. However, SRO observed in Ni-Cr binary systems [53,54] may also suggest possible SRO for the ternary. Also, long-range ordering and precipitation in Ni-Cr alloys ($MoPt_2$ type) [55–58], often discussed in combination with the K-state phenomena [56,59], indicate possible ordering for the multicomponent alloy at ambient temperatures too. Experimentally different conclusions were derived. For example, Yin *et al.* [60] demonstrated that the strength and hardness of CrCoNi samples prepared under different annealing conditions, and hence with presumably different degrees of SRO, were not affected by the potential presence of SRO. However, another experimental investigation by Zhang *et al.* [46] suggested a direct impact of SRO on the mechanical behavior of this alloy.

Computationally, Tamm *et al.* [43] first examined the presence of ordering in CrCoNi utilizing first-principles energy-based lattice Monte Carlo simulations. Their computational results suggested an increase of Cr-Co and Cr-Ni nearest neighbors at the expense of Cr-Cr pairs. Magnetic frustration has been suggested as a possible reason behind the observed Cr-Cr repulsion. The observed trend in ordering was qualitatively supported later by Zhang *et al.* [44] using x-ray and neutron total scattering and extended x-ray absorption fine structure techniques. Ding *et al.* [41] theoretically investigated the effect of SRO on the stacking fault energies in CrCoNi. They also found a similar trend of nearest-neighbor arrangement between different atom pairs as predicted by Tamm *et al.* [43]. However, those observations did not suggest a possible ordering of atoms in the alloy. Recently, Pei *et al.* [47] performed a cluster expansion for CrCoNi and proposed a possible FCC ground-state ordered structure with a special arrangement of alternating Cr rich layers and mixed Co and Ni atom layers. However, the calculated energy difference of around 31 meV/atom between the random structure and

*s.ghosh@mpie.de

possible ground state one proposed in [47] is smaller than the energy difference of around 45 meV/atom reported by Tamm *et al.* [43] This may suggest the existence of another, different low-energy ordering. A possible low-energy SRO state was also analyzed by Walsh *et al.* [49] via different types of SRO models, designed to minimize the magnetic energy by minimizing certain Cr spin interactions. It was concluded that a SRO model including specific magnetic configurations could explain the energy reduction suggested in [43].

In summary, though several studies have been devoted to revealing the role of SRO and phase stability in CrCoNi, some discrepancies still exist. The present work is dedicated to clarifying this and to providing over a wide temperature window SRO and phase stability and to analyzing the role of magnetism for it. For this purpose we have employed computationally efficient on-lattice machine learning interatomic potentials called low-rank potentials [36,61–63]. These types of potentials can accurately represent interactions in systems with many chemical components and can be combined with, e.g., Monte Carlo simulations. The potentials are trained on density functional theory (DFT) based supercell calculations and can achieve a DFT accuracy within a few meV per atom, including local lattice distortion effects.

II. METHOD AND COMPUTATIONAL DETAILS

As outlined in the introduction above, we employ the low-rank interatomic potential (LRP) [61] method, which is used as an interaction model in subsequent canonical Monte Carlo (MC) simulations in order to investigate short-range order and order-disorder phase transitions in the equiatomic CrCoNi system. The atomistic structure for the LRP model is represented as site occupancies on the ideal crystalline lattice. In this case, the FCC lattice sites are occupied by one of the atomic species, i.e., Cr, Co, or Ni.

For the LRPs, the total energy, E, for a given atomic configuration, σ, is defined as sum over the individual contributions of local environments as

$$E(\sigma) = \sum_{\xi \in \Omega} V(\sigma(\xi + r_1), \ldots, \sigma(\xi + r_n)), \tag{1}$$

where Ω is the lattice sites periodically repeated in space, V is the interatomic potential model in the tensor form, as described in Refs. [36,61–63], ξ is the position of a central atom, $\sigma(\xi + r_i)$ is the species of the ith site and r_i is the vector connecting the central site with the ith neighbor, and n is the number of closest neighbors in the environment, including the central atom ($n = 13$ in the FCC case). Local lattice distortions can be incorporated as long as the topology of the supercell remains the same, i.e., that each atom can be uniquely correlated with a given FCC lattice site.

The tensor V contains energy contributions of all possible atomic environments, namely, m^n environments, where m is the number of species in the system. Thus, for a FCC system with $m = 3$ species (Cr, Co, Ni) the tensor V consists of about 1.6 million parameters, which is completely unfeasible to obtain from quantum-mechanical data. In order to reduce the number of parameters, the low-rank tensor-train assumption is applied [36,61,62,64]. This reduces the number of parameters from m^n to nmr^2, where r is the rank of tensor V. The choice of the two adjustable parameters, the number of neighbors n and rank r, affects the predictive accuracy of the model. We considered the interaction of nearest neighbors, $n = 13$, and found $r = 5$ to be an optimal rank, resulting in about 900 parameters to be fitted.

The parameters are determined by solving the minimization problem with the following functional:

$$\frac{1}{K} \sum_{k=1}^{K} \mid E(\sigma^{(k)}) - E^{\mathrm{qm}}(\sigma^{(k)}) \mid^2, \tag{2}$$

where $\sigma^{(k)}$ are atomic configurations, the total number of which in the training set is denoted as K, and $E(\sigma^{(k)})$ and $E^{\mathrm{qm}}(\sigma^{(k)})$ are the energies of $\sigma^{(k)}$ predicted by LRP and calculated by DFT, correspondingly.

The dependence of V on its parameters is not linear. Thus, different local energy minima exist in the parameter space. Therefore, the minimization algorithm can find different local minima depending on the initial parameters. Different fits of LRPs hence provide independent energy predictions, and with a trained ensemble of several LRPs, the uncertainty level of the LRP model can be estimated.

The workflow as followed in our calculation procedure is the same as in Ref. [63]. First, a training set and validation set containing about 500 and 100 DFT energies of initially randomly generated configurations, each with 108 atoms, are prepared. Then an ensemble of 10 LRPs is trained, and the accuracy of them is checked with a separate validation dataset. With these LRPs Monte Carlo simulations are carried out on a 108 atom supercell, and values of the specific heat capacity for the LRP ensemble are compared for different temperatures. To improve the accuracy of the LRP, if needed, configurations corresponding to the temperature regime with larger deviations among the potentials in specific heat capacity are sampled and added to the training and validation set, and a new ensemble of 10 LRPs is trained. This procedure is continued until deviations in the predictions for the specific heat capacity calculated through different LRPs are reduced noticeably as discussed further in Sec. III. With the trained ensemble of LRPs, we proceed with MC simulations on larger supercells.

The configurations in the training sets are calculated with spin-polarized density functional theory (DFT) as implemented in Vienna Ab initio Simulation Package (VASP) 5.3.5 [65–67] in combination with the projector augmented wave method [68] and utilizing the Perdew-Burke-Ernzerhof generalized gradient approximation [69] for the exchange-correlation functional. A fixed lattice parameter of 3.55 Å is used, which is between the temperature $T = 0$ K theoretical and room temperature experimental lattice constants for CrCoNi [43,45,70,71]. The impact of volume relaxations will be discussed later. For the considered $3 \times 3 \times 3$ (108 atom) supercell an energy cutoff of 300 eV and a Monkhorst-Pack $4 \times 4 \times 4$ k-mesh was used for the self-consistent calculations. Ionic relaxations of atomic positions with a fixed cell volume and shape are included in the calculations. The convergence criteria for the total energies and the forces on individual atoms are set to 10^{-3} eV and 10^{-2} eV/Å, respectively. Electronic excitations are included by utilizing the Fermi distribution in the DFT calculations with a smearing

parameter of 0.1 eV. To include magnetism, each of the atomic configurations has been initialized with different random arrangements of magnetic spins to mimic magnetic disorder. This is justified due to the experimentally reported very low Curie temperature of around 4 K in this alloy [72,73].

The MC simulations are performed with periodic boundary conditions. We mainly focus on the temperature range 50–2000 K. The majority of simulations are carried out for systems with 108, 864, and 6912 atoms, i.e., $3 \times 3 \times 3$, $6 \times 6 \times 6$, and $12 \times 12 \times 12$ lattice units, based on a four-atom primitive FCC cell. The number of MC steps is 2×10^5 times the number of atoms in the corresponding lattice units. To achieve an unbiased averaging, the so-called burn-in approach [74] was implemented; i.e., for each temperature the first half of MC steps was neglected. This technique is necessary in the range of temperatures that include phase transitions but was used permanently in our calculations to improve the robustness of the algorithm.

The atomic structures were visualized with the VESTA software package [75].

III. RESULTS AND DISCUSSION

To evaluate the performance of the potentials and to detect possible phase transitions we first focus on the temperature dependency of the specific heat capacity, C_V, as obtained through canonical MC simulations. For the initial potential fitting a $3 \times 3 \times 3$ supercell containing 108 atoms is chosen, considering different chemically and magnetically random configurations. The variance in energies for different magnetic configurations for a fixed chemical configuration is in the order of a few meV, which is consistent with the low magnetic critical temperature reported experimentally [72,73]. We averaged over the magnetic degrees of freedom so that the potentials effectively fit a mean energy for each chemical configuration. We discuss the impact of magnetism on the observed ordered configurations also in detail at the end of this section. An ensemble of 10 LRPs is trained and used in subsequent Monte Carlo simulations. We included 500 configurations in the initial training set and validated on 100 separate configurations. The mean validation error of these initially trained LRPs was around 2.75 meV/atom as averaged over 10 LRPs with a standard deviation of 0.025 meV/atom. Thus, all 10 LRPs revealed comparable fitting errors. Using the ensemble of trained potentials we performed MC simulations and analyzed the dependency of the specific heat capacity on temperature as shown in Fig. 1(a). The same lattice cell size of $3 \times 3 \times 3$ (i.e., 108 atoms) was considered in the MC simulations as used for the actual DFT calculations entering the training set. These initially fitted potentials reveal two phase transitions which will be discussed further below. As can be seen in Fig. 1(a), for the initially fitted potentials, significant fluctuations were observed among the ten different LRP potentials near the transition region, i.e., around the peaks observed in the specific-heat capacity curve. Note that in this first training round, the potentials are only fitted to random configurations. For the retraining process, we sampled several new configurations within the range of temperatures 90 K to 1590 K with an interval of 60 K, including the regime near the observed phase transitions. We considered in this

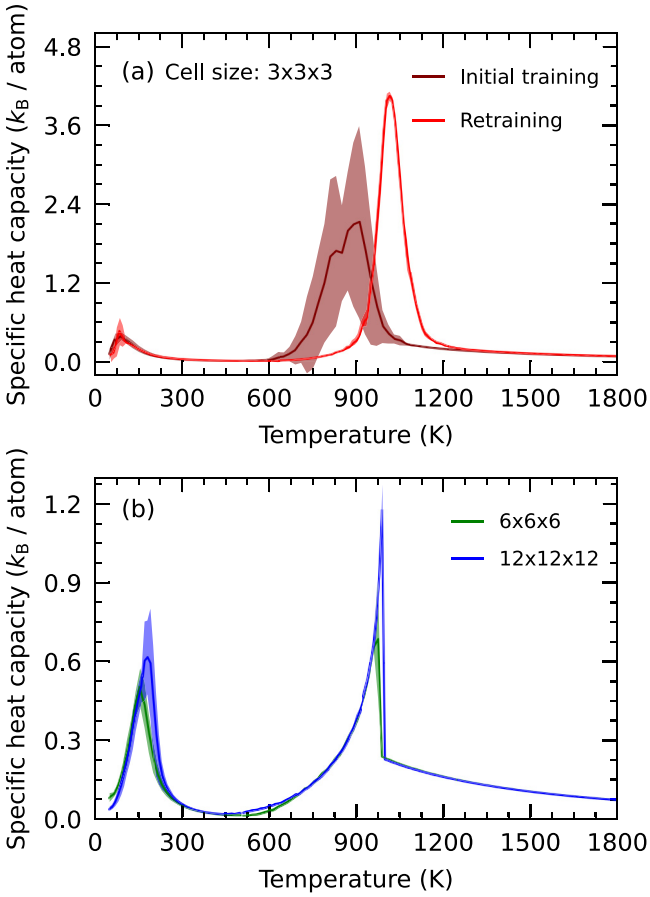

FIG. 1. The temperature dependence of specific-heat capacity C_V based on Monte Carlo simulation for an equiatomic FCC CrCoNi alloy with supercell size (a) $3 \times 3 \times 3$, i.e., 108 atoms (brown and red correspond to MC simulation results based on initially trained and retrained ensemble of 10 LRP potentials, respectively) and (b) for $6 \times 6 \times 6$ and $12 \times 12 \times 12$, i.e., 864 and 6912 atoms, respectively. The solid lines represent the averaged heat capacity over an ensemble of 10 LRPs, and the shaded area corresponds to the standard deviation of the LRPs ensemble.

retraining round three different initial magnetic configurations for each sampled chemical configuration corresponding to a particular temperature. As a result, 780 new configurations were considered from MC simulations and recalculated with DFT. The training and validation sets included 1180 and 200 configurations, respectively. The mean prediction error of the retrained LRPs was reduced to 2.36 meV/atom. Fluctuations in the specific heat curves among different LRPs were significantly reduced as shown in Fig. 1(a). This newly trained ensemble of 10 LRPs was then employed for further MC simulations with larger simulation cells. We carefully evaluated the convergence of the statistical parameters near the phase transitions by heating and cooling simulations as well as evaluating the impact of the number of MC steps as discussed in detail in Appendix A.

The temperature-dependent specific heat capacity, obtained for two larger supercell sizes of $6 \times 6 \times 6$ and $12 \times 12 \times 12$ containing 864 and 6912 atoms, is presented in Fig. 1(b). Again two characteristic peaks implying two

possible phase transitions are observed with decreasing temperature: a first transition is found around 975 K, and another one around 180 K. It is noteworthy that the observed peak around 975 K is in good agreement with previous experimentally observed anomalies at that temperature [76]. When increasing the system size from $3 \times 3 \times 3$ to a $6 \times 6 \times 6$ supercell, the high-temperature transition appears as a very sharp discontinuous transition, qualitatively different as compared to the low-temperature one. When further increasing the supercell size from $6 \times 6 \times 6$ to $12 \times 12 \times 12$, only minor variations in the heat capacity results are observed. We, therefore, proceed with our analysis based on $12 \times 12 \times 12$ supercell size calculations. In the following, we further analyze the nature of the phase transitions by inspecting the internal energy of the system.

The mean internal energies as a function of temperature and for the various employed supercell sizes are shown in Fig. 2(a) as obtained from our MC simulations. In addition to the energies we also show in Fig. 2 three characteristic configurations for the different temperature regimes: (1) a random structure obtained at very high temperature [see Fig. 2(d)], (2) an ordered structure referred to as $Cr(Co, Ni)_2$ [snapshot taken at 510 K, in Fig. 2(c)], and (3) another low-temperature, phase-separated one referred to as $CrCo_2 + CrNi_2$ [snapshot taken at 50 K, in Fig. 2(b)]. The order-disorder transition takes place at around 975 K [see Figs. 2(c) and 2(d)]. This ordering results into the observed sharp energy drop in Fig. 2(a). At even lower temperatures a second transition is observed into $CrCo_2 + CrNi_2$, where the ordering of Cr atoms remains the same; however, the Co and Ni atoms are separated [Fig. 2(b)]. Note that a proper ground state investigation at very low temperatures may further require the consideration of different lattice structures (e.g., body-centered cubic lattice for Cr), which is beyond the scope of the present work. Further, ordering phenomena at very low temperatures may be hard to realize experimentally due to kinetic limitations. In the following we, therefore, focus on the high-temperature phase transition.

For the ordered phases a special arrangement of constituent atomic layers exists. In a period of three parallel {110} or {113} layers, one layer is completely occupied with Cr atoms, and the other two contain Co and Ni atoms. We have identified this as the $MoPt_2$ ordering (with Immm symmetry), similar to Ni_2Cr ordering known for Ni-Cr alloys [55–57,77]. This ordering is better visualized using an orthorhombic primitive cell. Therefore we also performed additional MC simulations employing this cell. The $6 \times 6 \times 6$ supercell based on this primitive cell contains 1296 atoms. Equal numbers of Cr, Co, and Ni atoms are again randomly distributed on the lattice sites, and MC simulations are performed with the same set of LRPs. Snapshots from the simulations, taken at 50 K and 510 K, are depicted in Figs. 2(e) and 2(f), respectively. The snapshot at 510 K in Fig. 2(f) shows the same ordering arrangement as in case of cubic supercell in Fig. 2(c). The MC simulated temperature dependency of the internal energy for the orthorhombic supercell also has been compared to the cubic supercell in the inset of Fig. 2(a) revealing that both employed supercells provide consistent results.

To quantify the degree of ordering as well as the amount of SRO in the solid solution, the Warren-Cowley SRO

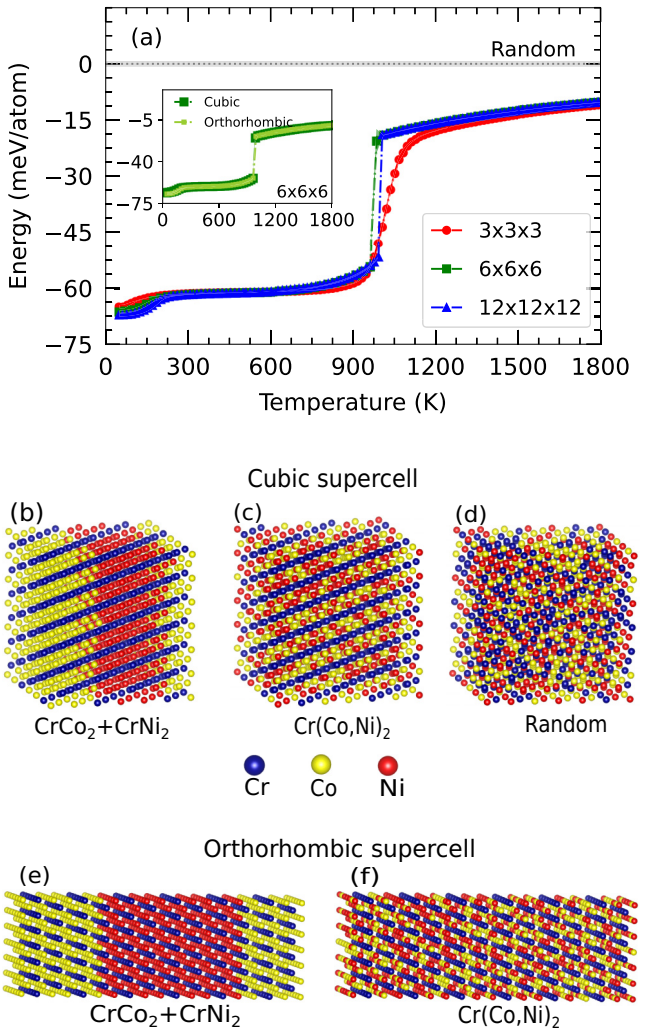

FIG. 2. In (a) the calculated temperature dependence of the mean internal energies from MC simulations for an equiatomic FCC CrCoNi alloy has been compared for different supercell sizes: $3 \times 3 \times 3$ (108 atoms), $6 \times 6 \times 6$ (864 atoms), and $12 \times 12 \times 12$ (6912 atoms) in the case of a cubic supercell. In the inset, the temperature-dependent internal energies from MC simulation on an orthorhombic supercell have been compared to that of a cubic one for $6 \times 6 \times 6$ supercell size. The structures containing 864 atoms (in the case of a cubic supercell) correspond to the (b) lower energy Co and Ni separated ordered structure at 50 K (referred to as $CrCo_2 + CrNi_2$), (c) ordered layered structure at 510 K (referred to as $Cr(Co, Ni)_2$), and (d) random solid solution (referred to as random) at very high temperature (left to right), respectively. The structures in (e) and (f) are the snapshots taken at 50 K and 510 K from MC simulation on the orthorhombic supercell with supercell size $6 \times 6 \times 6$ (1296 atoms) and are equivalent to $CrCo_2 + CrNi_2$ and $Cr(Co, Ni)_2$ structures, respectively. Energies in (a) are referenced to the energy of the random solid solution.

parameters [78] were calculated as

$$\alpha_{ij}^{m} = 1 - \frac{p_{ij}^{m}}{c_i c_j}, \tag{3}$$

where α_{ij}^{m} is the Warren-Cowley SRO parameter for the atomic types i and j at the mth coordination shell, p_{ij}^{m} is the

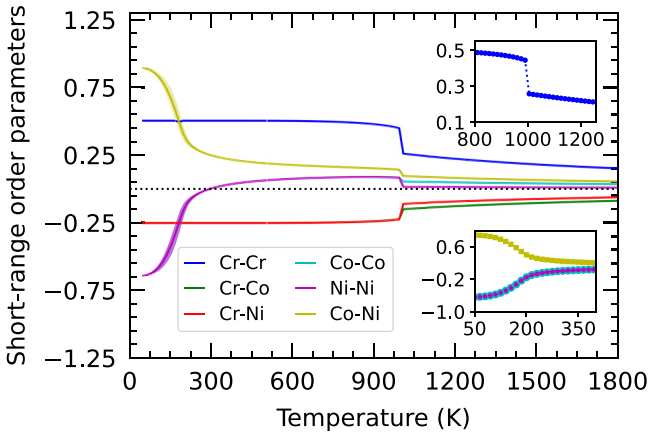

FIG. 3. Temperature-dependent Warren-Cowley SRO parameters for different atom pairs in the first coordination shell in an equiatomic CrCoNi alloy. The parameters from the MC simulations are averaged over an ensemble of 10 LRPs, and the light shaded areas show the standard deviation (uncertainty level) of the utilized LRPs. The insets show the qualitatively different nature of the low- (continuous) and high-temperature (discontinuous) transitions.

probability of finding atom type j at the mth coordination shell of atom i, and c_i, c_j are the concentrations of elements i and j in the alloy. According to this definition, positive (negative) values of the SRO parameter at the mth coordination shell mean that atoms i and j avoid (attract) each other at the corresponding coordination shell.

The computed SRO parameters as a function of temperature for different atom pairs in the first coordination shell (i.e., $m = 1$) are shown in Fig. 3. At temperatures above 975 K, a positive value of $\alpha_{\text{Cr-Cr}}$ indicates Cr-Cr repulsion in the first nearest-neighbor shell, whereas negative values of $\alpha_{\text{Cr-(Co, Ni)}}$ indicate a preference for Cr atoms to bond with Co and Ni atoms. These tendencies become more prominent below the high-temperature transition around 975 K where also the $\alpha_{\text{Cr-Cr}}$ shows an abrupt change. The corresponding $\alpha_{\text{Cr-Cr}}$ value saturates at a value of 0.5 implying a strong repulsion of Cr-Cr first neighboring pairs. This is consistent with the ordered Cr(Co, Ni)_2 structure observed as shown in Fig. 2(c) [or Fig. 2(f)]. Besides Cr-Cr ordering, the number of Cr-(Co, Ni) atom pairs increases below 975 K as indicated by the increased negative values of $\alpha_{\text{Cr}-\text{(Co,Ni)}}$. The similar SRO parameters for Cr-Co and Cr-Ni also indicate similar interactions for Cr with Ni and Co, thus supporting the low-temperature separation of CrCoNi into Cr(Co, Ni)_2 and $\text{CrCo}_2 + \text{CrNi}_2$, respectively. We, therefore, conclude that the high-temperature phase transition manifested in the first peak in the specific heat curve at 975 K [Fig. 1(b)] is mainly driven by the ordering of the Cr atoms. The low-temperature phase transition, the origin of the second peak in the heat capacity, is clearly driven by the significant change in $\alpha_{\text{Co-Co}}$, $\alpha_{\text{Ni-Ni}}$, and $\alpha_{\text{Co-Ni}}$ values corresponding to the phase separation of Co and Ni in the alloy as visualized in Fig. 2(b). At the same time, the ordering of Cr atoms remains almost the same in this temperature regime indicating that the second phase transition is mainly driven by Co and Ni. A good qualitative agreement is revealed for the computed SRO parameters

TABLE I. Presently calculated low rank potential (LRP) based Monte Carlo (MC) simulated Warren-Cowley SRO parameters in CrCoNi alloy at a temperature of 500 K compared to previous DFT-based Monte Carlo studies by Tamm *et al.* [43] and Ding *et al.* [45].

Neighbor atoms pair	Present calculation LRP MC	Tamm *et al.* [43] DFT MC	Ding *et al.* [45] DFT MC
Cr-Cr	0.50	0.42	0.40
Cr-Co	−0.25	−0.16	−0.25
Cr-Ni	−0.25	−0.27	−0.15
Co-Co	0.06	0.01	0.06
Ni-Ni	0.06	0.12	−0.04
Co-Ni	0.19	0.15	0.19

(in the ordered configuration) at 500 K while compared with those from previous works [43,45] as shown in Table I.

Although the first nearest-neighbor correlation functions qualitatively agree with previous works, some discrepancies are observed comparing the ordering energies as referenced to the energy of the random solid solution. The ordered configuration suggested in [47] is about 31 meV/atom lower in energy as compared to the random one. In another computational study, by employing a combination of DFT and MC simulations, Tamm *et al.* [43] found an energy difference of 45.7 meV/atom at 500 K. This already suggests that the ordered configuration proposed in [47] is likely not the energetically most favorable one. Indeed, the energy difference for Cr-layered ordered Cr(Co, Ni)_2 structure found in the present work below 975 K is about 60 meV/atom; see also Fig. 2(a).

To rule out any possible fitting error we have reevaluated the LRP-predicted structures again with explicit DFT calculations. We performed for each scenario 30 calculations, which include 10 different MC snapshots obtained from the 10 independently fitted LRP-based MC simulations and three different initial magnetic configurations for each of them. We considered the $\text{CrCo}_2 + \text{CrNi}_2$, Cr(Co, Ni)_2 and random structures. All energy differences for $\text{CrCo}_2 + \text{CrNi}_2$ and Cr(Co, Ni)_2 structures with respect to the random one are shown in Fig. 4 and compared to those of the ordered phases proposed in previous studies. The error bars indicate the standard deviation for the averaged computed DFT values for each case. We also evaluated the impact of volume relaxation as well as the inclusion of electronic excitations using a Fermi smearing of 0.1 eV corresponding to 1160 K. For every considered scenario, the here proposed ordered Cr(Co, Ni)_2 structure is found to be significantly lower in energy compared with previous results.

Next, we analyze and compare the ordered structure in Fig. 2(c) [or Fig. 2(f)] to the one proposed in [47] to further rationalize the reason behind the energetic difference. The structures are shown in Fig. 5. As shown in Fig. 5(c), Pei *et al.* [47] suggested a ground-state-ordered structure with Cr occupying a complete {002} layer and Ni and Co sharing the other two layers in a period of three layers. An almost similar tendency in the arrangement of atomic layers is observed in our case [see Figs. 5(a) and 5(b)]; i.e., in a period of three atomic layers, one layer is completely occupied with Cr atoms, and the subsequent two layers are occupied with

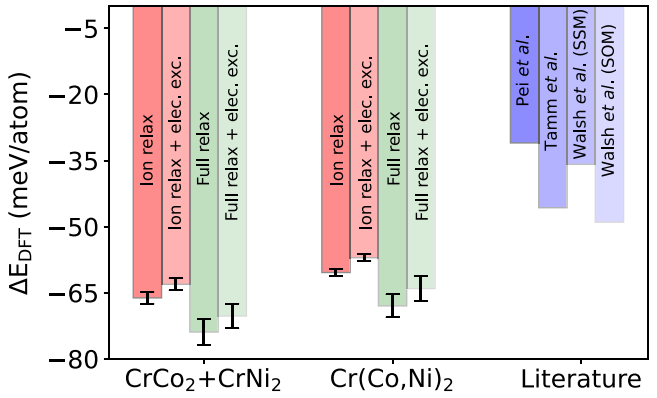

FIG. 4. DFT calculated energy differences as compared to a fully random state for the two ordered states, $CrCo_2 + CrNi_2$ and $Cr(Co, Ni)_2$, found in the present work [see also Figs. 2(c) and 2(d)]. The calculations include ionic relaxations (red) as well as volume and cell shape relaxations, i.e., full relaxation (green). The impact of electronic excitations (light red and light green) is shown as well. The DFT calculated energy differences found in previous literature results (blue shades) by Pei *et al.* [47], Tamm *et al.* [43], and Walsh *et al.* [49] between the random state and their proposed ordered state also have been added and compared to our thermodynamic equilibrium computed ordered configurations.

mixed Co and Ni atoms as shown for both considered cubic and orthorhombic supercell types. However, the remarkable difference is that in contrast to Fig. 5(c), in Figs. 5(a) and 5(b) each Cr atom shares only two nearest-neighbor Cr atoms, also consistent with the saturated value of $\alpha_{\text{Cr-Cr}}$ in Fig. 3. This may favor magnetic contributions as previous investigations on CrCoNi suggested that the frustration of antiferromagnetic Cr can be greatly relieved by minimizing the number of Cr-Cr nearest neighbors.

In the following, we further analyze the magnetic contributions. In a previous study, Walsh *et al.* [49] argued that the origin of the more than 40 meV/atom reduction in energy in the ordered phase found by Tamm *et al.* [43] may be explained by a combination of chemical SRO and minimization of the magnetic frustration effects. According to their study, Co atoms align ferromagnetically, while local magnetic moments of Ni atoms are suppressed; Cr atoms prefer to magnetize antiferromagnetically with respect to Co, however, avoiding like-spin Cr atoms. To understand the situation in our presently proposed ordered structure, we visualize in Fig. 6(a) the magnetic alignment of atoms for an exemplary ordered configuration calculated with spin-polarized DFT on a 108-atom cell. Indeed, some of the Co atoms and all Ni atoms have almost zero local magnetic moments. All other Co atoms are aligned ferromagnetically and the Cr atoms, which are nearest neighbors to these ferromagnetic Co atoms, either have zero or reveal an antiparallel magnetic moment. Other than that, either one of the two nearest-neighbor Cr atoms possesses zero local moment, otherwise those are antiferromagnetically aligned, whereas second nearest-neighbor Cr atoms are ferromagnetically aligned. Thus the preferences found for the magnetic alignments are in good agreement with the ones found in [49]. A detailed distribution of the local magnetic moments for Cr, Co, and Ni atom types in the

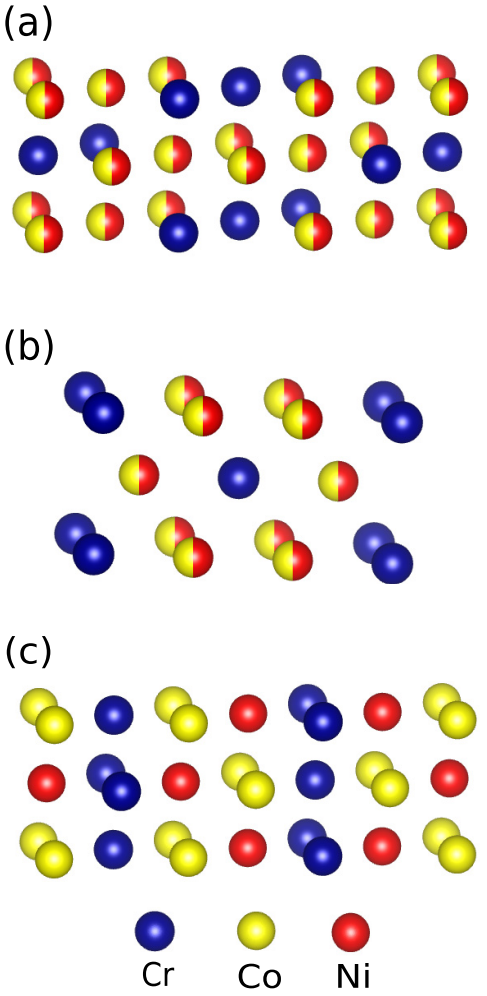

FIG. 5. The arrangement of constituent atoms in (a) the here obtained ordered structure (in the case of cubic supercell) of CrCoNi at a temperature of 510 K compared with (c) the ground state structure as suggested by Pei *et al.* [47]. In the case of (a), for clear visualization of our obtained $Cr(Co, Ni)_2$ structure, only a certain part of the 864-atom cell with a smaller boundary is shown. Another orthorhombic primitive cell (also see Appendix C) as considered in the case of orthorhombic supercell for $Cr(Co, Ni)_2$ structure also has been added in (b) for better visualization. The half-colored spheres with yellow and red represent the 50% occupancy probability of Co and Ni atoms for those sites.

random and ordered states is shown in Fig. 9 in Appendix B. On the other hand, our spin-polarized DFT calculations for the structure shown in Fig. 5(c) reveal possibilities of magnetic frustration in the structure [see Fig. 6(b)]. Some of the nearest-neighbor Co-Cr atoms are antiparallelly aligned, whereas some of them are parallel. This may be a reason that the configuration in Fig. 5(c) is energetically higher than the one found in the present work [Fig. 5(a) or 5(b)].

Therefore, we finally evaluated the impact of magnetic energies on the observed ordering, i.e., whether magnetism drives the ordering or just adapts for a given chemical configuration. As mentioned in the beginning, the difference in magnetic energies as obtained from different magnetic structures while keeping the chemical configuration fixed revealed

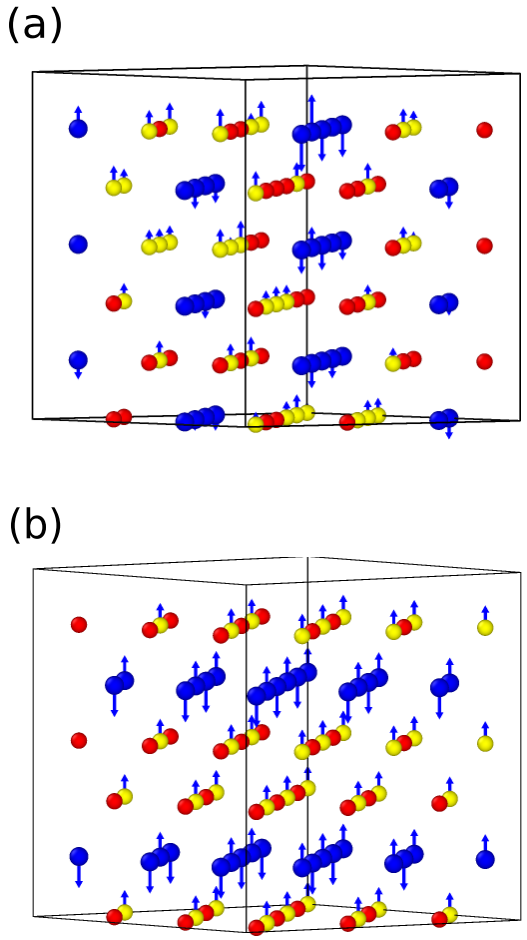

FIG. 6. The alignment of local magnetic moments in (a) our here proposed ordered $Cr(Co, Ni)_2$ structure of CrCoNi compared with (b) the one proposed in [47], both calculated with spin-polarized DFT for a 108-atom cell. Blue, yellow, and red spheres represent Cr, Co, and Ni atoms, respectively. Visualization is performed with the OVITO software [79].

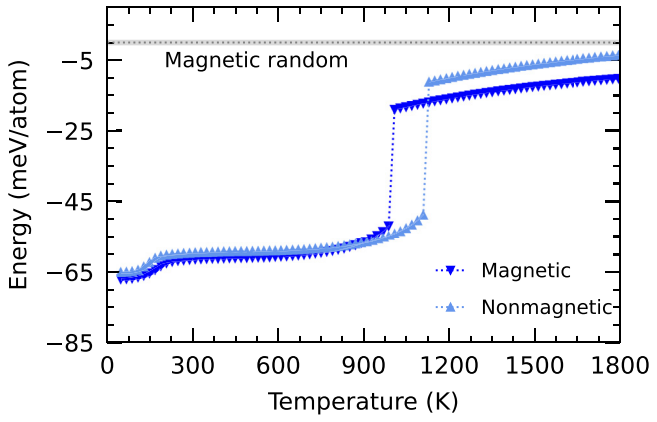

FIG. 7. The calculated temperature dependence of mean internal energies obtained from magnetic and nonmagnetic LRP-based MC simulations for an equiatomic CrCoNi alloy with supercell size $12 \times 12 \times 12$. The energy of high-temperature magnetic random solid solution has been included as reference (gray line).

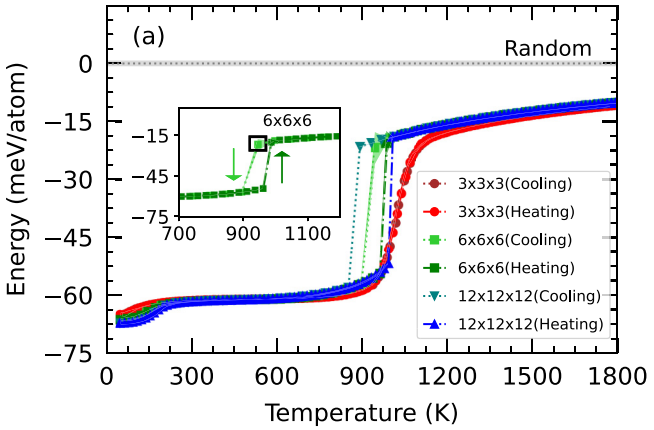

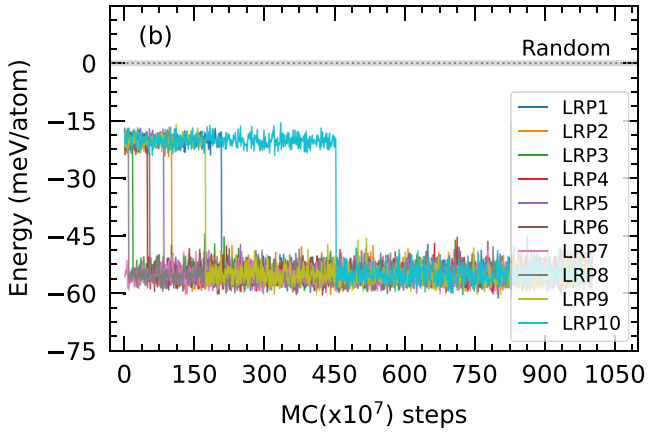

FIG. 8. In (a) the calculated temperature dependence of the mean internal energies from heating and cooling MC simulations for an equiatomic FCC CrCoNi alloy are compared for different supercell sizes: $3 \times 3 \times 3$ (108 atoms), $6 \times 6 \times 6$ (864 atoms), and $12 \times 12 \times 12$ (6912 atoms) with 2×10^5 number of MC steps. In the inset, the observed hysteresis in the case of a $6 \times 6 \times 6$ (864 atoms) supercell is shown near the high-temperature phase transition. In (b) the convergence of the internal energy with the number of MC steps is shown. A temperature of 945 K, which is in the hysteresis region [marked by a square in the inset of (a)], is used in the simulations. The calculations are performed in a $6 \times 6 \times 6$ supercell and taken for each of the fitted 10 LRPs. Energies are referenced to the energy of the random solid solution.

very weak magnetic contributions. One possibility may be therefore that, although the local magnetic moments are optimized and minimize magnetic frustration for a given chemical state, the magnetism is itself not the driving force to determine the chemical ordering. Therefore, to investigate whether magnetism in the alloy is introducing the chemical arrangement of atoms obtained in our ordered structure, we fully separated the magnetic degrees of freedom for the entire investigation. We repeated the whole procedure of preparing training and validation sets with non-spin-polarized DFT calculations and then trained a new ensemble of 10 LRPs. With those potentials, we rerun the Monte Carlo simulation to investigate ordering in the system. The temperature dependency of mean total energy obtained in MC simulation is shown in Fig. 7 compared with the previous magnetic calculation. Indeed, the

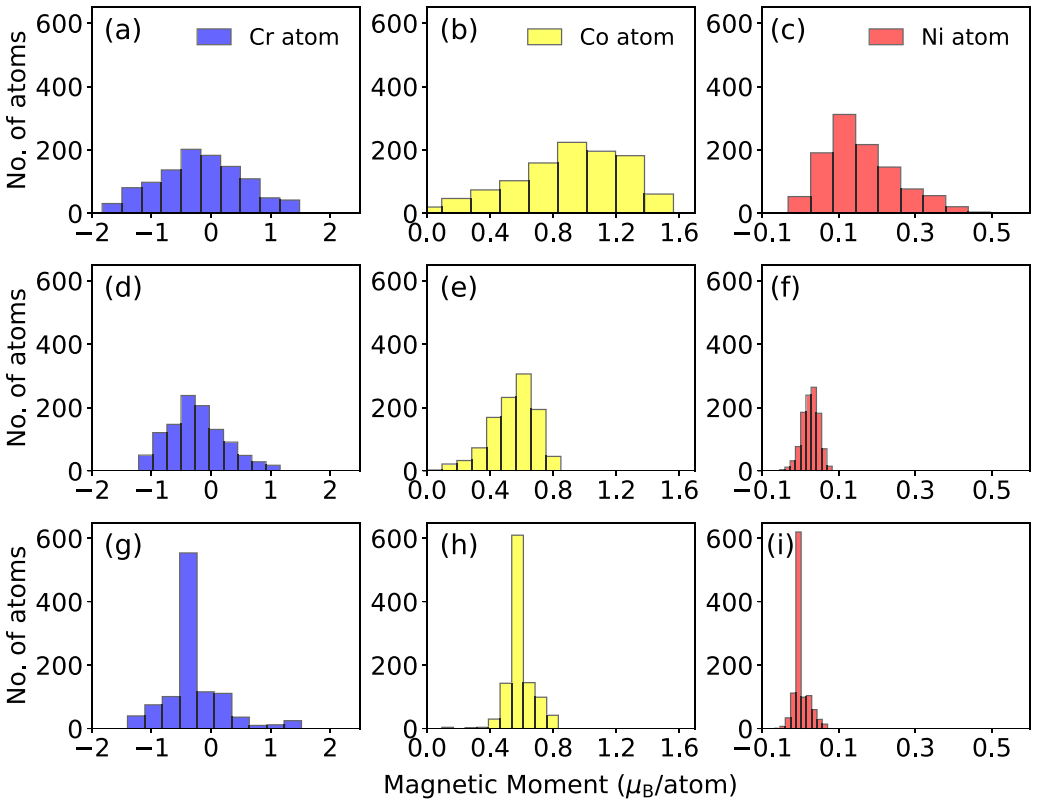

FIG. 9. The moment distribution for the three different atom types Cr, Co, and Ni in the three different structures: [(a)–(c)] random, [(d)–(f)] ordered $Cr(Co, Ni)_2$, and [(g)–(i)] ordered $CrCo_2 + CrNi_2$ structures.

total energy remains almost the same in the ordered region below 900 K, with a slight shift in the transition temperature. While observing the chemical arrangement in the ordered structure, the ordering trend remains the same as obtained from our spin-polarized calculations. We, therefore, conclude that although the magnetic state is optimized and relieves magnetic frustration in a given chemical state, which on first glance may suggest magnetism is crucial to understanding the ordering in this alloy, magnetism is actually not responsible for the ground-state ordering. However, we note that finite-temperature magnetic fluctuations or kinetic considerations, not included in the present work, could in principle also impact the ordering.

IV. SUMMARY

We have investigated SRO and phase stability in CrCoNi employing on-lattice machine learning interatomic potentials and canonical Monte Carlo simulations. On the FCC lattice, a first-order order-disorder transition from a high-temperature random structure to an ordered one is observed around 975 K, manifested in a discontinuous peak in the specific heat capacity. The ordered structure is identified as $Cr(Co, Ni)_2$ ($MoPt_2$-type), similar to Ni_2Cr ordering known for Ni-Cr alloys. In $Cr(Co, Ni)_2$ the arrangement of Cr atoms is such that each Cr atom has only two nearest-neighboring Cr atoms. The energy of this predicted ordered structure is almost twice lower in energy than those found in previous simulations. Phase separation at low temperature (around 180 K) into $CrCo_2 + CrNi_2$ with the same $MoPt_2$ type of ordering is also observed. The impact of magnetism on the observed ordering is found to be negligible, and even nonmagnetic DFT calculations predict the same type of ordering. This suggests that magnetism, though being itself affected, is not the driving force in determining the ground-state ordering in CrCoNi.

ACKNOWLEDGMENTS

S.G. and F.K. appreciate fruitful discussions with Marcel Sluiter. S.G., F.K., and A.S. acknowledge support from a collaborative DFG-RFBR grant (Grants No. DFG KO 5080/3-1 and No. RFBR 20-53-12012).

APPENDIX A: CONVERGENCE NEAR THE HIGH-TEMPERATURE PHASE TRANSITION

After performing cooling simulations and having the ordered structures, we also performed heating Monte Carlo simulations for all employed cubic supercells, i.e., $3 \times 3 \times 3$ (108 atoms), $6 \times 6 \times 6$ (864 atoms), and $12 \times 12 \times 12$ (6912 atoms), as shown in Fig. 8. With the provided number of MC steps, we observed no hysteresis for $3 \times 3 \times 3$ supercell. However, with increasing supercell size, hysteresis is obtained for both $6 \times 6 \times 6$ and $12 \times 12 \times 12$ supercells around the high-temperature first-order phase transition regime. For example, for a $12 \times 12 \times 12$ supercell, the transition temperature is about 975 K for a heating simulation and is about 150 K lower if cooled from higher temperatures using the same number of MC steps. Therefore, we carefully evaluated the convergence near the phase transition by increasing the

number of MC steps. For this purpose, we picked an intermediate temperature structure from the hysteresis interval for a $6 \times 6 \times 6$ supercell, as shown in the inset of Fig. 8(a), and increased the number of Monte Carlo steps in the simulations for each of the potentials. We increased the number of MC steps by five orders of magnitude from 2×10^5 to 10^{10} MC steps (swap attempts per atom in the supercell). The corresponding energies are shown in Fig. 8(b) (note the scaling of the x axis). For this selected temperature in the hysteresis regime, all fitted LRPs used for $6 \times 6 \times 6$ sized supercells, though running initially for 2×10^5 MC steps, provide system energies in the higher energy disordered state but finally converge down to the lower energy ordered state as observed in case of heating simulations [see inset of Fig. 8(a)]. We thus conclude that the observed hysteresis is rather an artifact of the number of MC steps and that the thermodynamic stable solution in the hysteresis regime is the ordered phase. Note, however, the extremely long simulation times needed if the MC simulations were performed only starting from a random solution.

APPENDIX B: LOCAL MOMENTS DISTRIBUTION

The distributions of local moments for Cr, Co, and Ni atoms in different structures are analyzed in Fig. 9. In the random structures a broad distribution of moments for the atoms is observed due to the variety of different local chemical environments. In the ordered $Cr(Co, Ni)_2$ structure, the magnitude of the moments gets minimized. All the Co atoms have a positive moment value, whereas for Cr atoms the distribution is from -1.0 to 1.0. This reflects the findings in Fig. 6(a) that in ordered $Cr(Co, Ni)_2$ structure nearest-neighbor Co-Co are parallelly aligned, Co-Cr are antiparallelly aligned, and second nearest-neighbor Co-Cr and Cr-Cr are parallelly aligned and some of the Cr atoms have almost zero moment. Ni atoms attain almost zero moments in the ordered states. For the low-temperature phase-separated $CrCo_2 + CrNi_2$ configurations, the distribution becomes sharper.

APPENDIX C: COORDINATES OF ORTHORHOMBIC PRIMITIVE CELL

The primitive orthorhombic cell in Fig. 5(b) can be realized with, e.g., the POSCAR as shown below.

```
CrCoNi
1.00
0.0 0.0 3.55
1.775 -1.775 0.0
5.325 5.325 0.0
Cr Co Ni
2 2 2
Cartesian
0.00000000 0.00000000 0.00000000
3.55000000 1.77500000 1.77500000
1.77500000 1.77500000 0.00000000
3.55000000 3.55000000 0.00000000
1.77500000 0.00000000 1.77500000
5.32500000 3.55000000 1.77500000
```


[1] J.-W. Yeh, S.-K. Chen, S.-J. Lin, J.-Y. Gan, T.-S. Chin, T.-T. Shun, C.-H. Tsau, and S.-Y. Chang, Adv. Eng. Mater. **6**, 299 (2004).

[2] B. Cantor, I. Chang, P. Knight, and A. Vincent, Mater. Sci. Eng. A **375–377**, 213 (2004).

[3] Y. Zhang, X. Yang, and P. Liaw, JOM **64**, 830 (2012).

[4] Y. Zhang, Y. J. Zhou, J. P. Lin, G. L. Chen, and P. K. Liaw, Adv. Eng. Mater. **10**, 534 (2008).

[5] C. Li, J. Li, M. Zhao, and Q. Jiang, J. Alloys Compd. **475**, 752 (2009).

[6] F. Otto, Y. Yang, H. Bei, and E. P. George, Acta Mater. **61**, 2628 (2013).

[7] D. B. Miracle and O. N. Senkov, Acta Mater. **122**, 448 (2017).

[8] E. P. George, D. Raabe, and R. O. Ritchie, Nat. Rev. Mater. **4**, 515 (2019).

[9] O. Senkov, J. Scott, S. Senkova, D. Miracle, and C. Woodward, J. Alloys Compd. **509**, 6043 (2011).

[10] M.-H. Chuang, M.-H. Tsai, W.-R. Wang, S.-J. Lin, and J.-W. Yeh, Acta Mater. **59**, 6308 (2011).

[11] M. A. Hemphill, T. Yuan, G. Wang, J. Yeh, C. Tsai, A. Chuang, and P. Liaw, Acta Mater. **60**, 5723 (2012).

[12] T.-t. Zuo, S.-b. Ren, P. K. Liaw, and Y. Zhang, Int. J. Miner. Metall. Mater. **20**, 549 (2013).

[13] Z. Tang, M. C. Gao, H. Diao, T. Yang, J. Liu, T. Zuo, Y. Zhang, Z. Lu, Y. Cheng, Y. Zhang *et al.*, JOM **65**, 1848 (2013).

[14] J. Antonaglia, X. Xie, Z. Tang, C.-W. Tsai, J. Qiao, Y. Zhang, M. Laktionova, E. Tabachnikova, J. Yeh, O. Senkov *et al.*, JOM **66**, 2002 (2014).

[15] Y. Zhang, T. Zuo, Y. Cheng, and P. K. Liaw, Sci. Rep. **3**, 1455 (2013).

[16] M. Laktionova, E. Tabchnikova, Z. Tang, and P. Liaw, Low Temp. Phys. **39**, 630 (2013).

[17] A. Gali and E. P. George, Intermetallics **39**, 74 (2013).

[18] B. Gludovatz, A. Hohenwarter, D. Catoor, E. H. Chang, E. P. George, and R. O. Ritchie, Science **345**, 1153 (2014).

[19] Y. Deng, C. C. Tasan, K. G. Pradeep, H. Springer, A. Kostka, and D. Raabe, Acta Mater. **94**, 124 (2015).

[20] Z. Li, K. G. Pradeep, Y. Deng, D. Raabe, and C. C. Tasan, Nature (London) **534**, 227 (2016).

[21] Z. Lei, X. Liu, Y. Wu, H. Wang, S. Jiang, S. Wang, X. Hui, Y. Wu, B. Gault, P. Kontis *et al.*, Nature (London) **563**, 546 (2018).

[22] P. Wu, K. Gan, D. Yan, Z. Fu, and Z. Li, Corrosion Sci. **183**, 109341 (2021).

[23] C. Niu, A. Zaddach, A. Oni, X. Sang, J. Hurt III, J. LeBeau, C. Koch, and D. Irving, Appl. Phys. Lett. **106**, 161906 (2015).

[24] S. Mu, J. Yin, G. D. Samolyuk, S. Wimmer, Z. Pei, M. Eisenbach, S. Mankovsky, H. Ebert, and G. M. Stocks, Phys. Rev. Mater. **3**, 014411 (2019).

[25] Z. Rao, B. Dutta, F. Körmann, D. Ponge, L. Li, J. He, L. Stephenson, L. Schäfer, K. Skokov, O. Gutfleisch *et al.*, Phys. Rev. Mater. **4**, 014402 (2020).

[26] Y. Zhang, Y. Zhuang, A. Hu, J.-J. Kai, and C. T. Liu, Scr. Mater. **130**, 96 (2017).

[27] Y. Ikeda, F. Körmann, I. Tanaka, and J. Neugebauer, Entropy **20**, 655 (2018).

[28] S. Zhao, Y. Osetsky, G. M. Stocks, and Y. Zhang, npj Comput. Mater. **5**, 1 (2019).

[29] Q.-J. Li, H. Sheng, and E. Ma, Nat. Commun. **10**, 1 (2019).

[30] E. Antillon, C. Woodward, S. Rao, B. Akdim, and T. Parthasarathy, Acta Mater. **190**, 29 (2020).

[31] D. King, S. Middleburgh, L. Edwards, G. Lumpkin, and M. Cortie, JOM **67**, 2375 (2015).

[32] M. Widom, W. P. Huhn, S. Maiti, and W. Steurer, Metal. Mater. Trans. A **45**, 196 (2014).

[33] S. Maiti and W. Steurer, Acta Mater. **106**, 87 (2016).

[34] Y. Wu and D. L. Irving, Appl. Phys. Lett. **119**, 111901 (2021).

[35] S. Zhao, J. Phase Equilibria Diffusion **42**, 578 (2021).

[36] T. Kostiuchenko, A. V. Ruban, J. Neugebauer, A. Shapeev, and F. Körmann, Phys. Rev. Mater. **4**, 113802 (2020).

[37] P. Singh, A. V. Smirnov, and D. D. Johnson, Phys. Rev. B **91**, 224204 (2015).

[38] X. Chen, Q. Wang, Z. Cheng, M. Zhu, H. Zhou, P. Jiang, L. Zhou, Q. Xue, F. Yuan, J. Zhu *et al.*, Nature (London) **592**, 712 (2021).

[39] B. Schönfeld, C. R. Sax, J. Zemp, M. Engelke, P. Boesecke, T. Kresse, T. Boll, T. Al-Kassab, O. E. Peil, and A. V. Ruban, Phys. Rev. B **99**, 014206 (2019).

[40] Y. Ma, Q. Wang, C. Li, L. J. Santodonato, M. Feygenson, C. Dong, and P. K. Liaw, Scr. Mater. **144**, 64 (2018).

[41] Q. Ding, Y. Zhang, X. Chen, X. Fu, D. Chen, S. Chen, L. Gu, F. Wei, H. Bei, Y. Gao *et al.*, Nature (London) **574**, 223 (2019).

[42] S. Yang, M. Jiang, H. Li, Y. Liu, and L. Wang, Rare Metals **31**, 75 (2012).

[43] A. Tamm, A. Aabloo, M. Klintenberg, M. Stocks, and A. Caro, Acta Mater. **99**, 307 (2015).

[44] F. X. Zhang, S. Zhao, K. Jin, H. Xue, G. Velisa, H. Bei, R. Huang, J. Y. P. Ko, D. C. Pagan, J. C. Neuefeind *et al.*, Phys. Rev. Lett. **118**, 205501 (2017).

[45] J. Ding, Q. Yu, M. Asta, and R. O. Ritchie, Proc. Natl. Acad. Sci. USA **115**, 8919 (2018).

[46] R. Zhang, S. Zhao, J. Ding, Y. Chong, T. Jia, C. Ophus, M. Asta, R. O. Ritchie, and A. M. Minor, Nature (London) **581**, 283 (2020).

[47] Z. Pei, R. Li, M. C. Gao, and G. M. Stocks, npj Comput. Mater. **6**, 1 (2020).

[48] K. Inoue, S. Yoshida, and N. Tsuji, Phys. Rev. Mater. **5**, 085007 (2021).

[49] F. Walsh, M. Asta, and R. O. Ritchie, Proc. Natl. Acad. Sci. USA **118**, e2020540118 (2021).

[50] S. Rideout, W. Manly, E. Kamen, B. Lement, and P. A. Beck, JOM **3**, 872 (1951).

[51] G. Zhmurko, E. Kabanova, V. Kuznetsov, and A. Leonov, Moscow Univ. Chem. Bull. **63**, 234 (2008).

[52] T. Omori, J. Sato, K. Shinagawa, I. Ohnuma, K. Oikawa, R. Kainuma, and K. Ishida, J. Phase Equilib. Diffus. **35**, 178 (2014).

[53] W. Schweika and H.-G. Haubold, Phys. Rev. B **37**, 9240 (1988).

[54] B. Schönfeld, L. Reinhard, G. Kostorz, and W. Bührer, Phys. Status Solidi B **148**, 457 (1988).

[55] M. Hirabayashi, M. Koiwa, K. Tanaka, T. Tadaki, T. Saburi, S. Nenno, and H. Nishiyama, Trans. Jpn. Inst. Met. **10**, 365 (1969).

[56] A. Marucco, Key Eng. Mat. **48**, 77 (1991).

[57] F. Teng, D. J. Sprouster, G. A. Young, J.-H. Ke, and J. D. Tucker, Materialia **8**, 100453 (2019).

[58] B. Stephan, D. Jacob, F. Delabrouille, and L. Legras, in *Proceedings of the 18th International Conference on Environmental Degradation of Materials in Nuclear Power Systems–Water Reactors*, edited by J. H. Jackson, D. Paraventi, M. Wright (Springer, Cham, 2019), pp. 233–249.

[59] A. Marucco and B. Nath, J. Mater. Sci. **23**, 2107 (1988).

[60] B. Yin, S. Yoshida, N. Tsuji, and W. Curtin, Nat. Commun. **11**, 2507 (2020).

[61] A. Shapeev, Comput. Mater. Sci. **139**, 26 (2017).

[62] E. A. Meshkov, I. I. Novoselov, A. V. Shapeev, and A. V. Yanilkin, Intermetallics **112**, 106542 (2019).

[63] T. Kostiuchenko, F. Körmann, J. Neugebauer, and A. Shapeev, npj Comput. Mater. **5**, 55 (2019).

[64] I. V. Oseledets, SIAM J. Sci. Comput. **33**, 2295 (2011).

[65] G. Kresse and J. Hafner, Phys. Rev. B **47**, 558 (1993).

[66] G. Kresse and J. Hafner, Phys. Rev. B **49**, 14251 (1994).

[67] G. Kresse and J. Furthmüller, Comput. Mater. Sci. **6**, 15 (1996).

[68] P. E. Blöchl, Phys. Rev. B **50**, 17953 (1994).

[69] J. P. Perdew, K. Burke, and M. Ernzerhof, Phys. Rev. Lett. **77**, 3865 (1996).

[70] S. S. Sohn, A. Kwiatkowski da Silva, Y. Ikeda, F. Körmann, W. Lu, W. S. Choi, B. Gault, D. Ponge, J. Neugebauer, and D. Raabe, Adv. Mater. **31**, 1807142 (2019).

[71] G. Laplanche, A. Kostka, C. Reinhart, J. Hunfeld, G. Eggeler, and E. George, Acta Mater. **128**, 292 (2017).

[72] K. Jin, B. C. Sales, G. M. Stocks, G. D. Samolyuk, M. Daene, W. J. Weber, Y. Zhang, and H. Bei, Sci. Rep. **6**, 20159 (2016).

[73] D. Billington, A. D. N. James, E. I. Harris-Lee, D. A. Lagos, D. ONeill, N. Tsuda, K. Toyoki, Y. Kotani, T. Nakamura, H. Bei *et al.*, Phys. Rev. B **102**, 174405 (2020).

[74] M. K. Cowles and B. P. Carlin, J. Am. Stat. Assoc. **91**, 883 (1996).

[75] K. Momma and F. Izumi, J. Appl. Crystallogr. **44**, 1272 (2011).

[76] K. Jin, S. Mu, K. An, W. D. Porter, G. D. Samolyuk, G. M. Stocks, and H. Bei, Mater. Des. **117**, 185 (2017).

[77] J. Buršık and M. Svoboda, Scr. Mater. **39**, 1107 (1998).

[78] J. Cowley, Phys. Rev. **120**, 1648 (1960).

[79] A. Stukowski, Modell. Simul. Mater. Sci. Eng. **18**, 015012 (2010).